Analytical and Bioanalytical Chemistry
https://doi.org/10.1007/s00216-026-06729-2

RESEARCH PAPER

Encapsulating acetylcholinesterase (AChE) into metal–organic frameworks for selective and sensitive colorimetric detection of carbaryl residue in water samples

Nor Khairun Bariah Kamaruddin[1] · Adila Mohamad Jaafar[2,3] · Fazira Ilyana Abdul Razak[4,6] · Suhaila Sapari[5] · Shahrul Ainliah Alang Ahmad[1,2]

Received: 5 May 2026 / Revised: 29 July 2026 / Accepted: 31 July 2026

Abstract

This study presents the development of an AChE@ZIF-8 composite biosensor using a gold nanoparticle (AuNPs) probe as a naked-eye signal readout platform for the sensitive detection of carbamate pesticides. As a biomarker for carbaryl monitoring, we present the encapsulation of acetylcholinesterase within zeolitic imidazolate frameworks-8 (AChE@ZIF-8) to enhance its stability without losing its intended functions. In this research, synthesis work of AChE@ZIF-8 was carried out using a biomineralization approach and characterized by Powder X-ray Diffraction (PXRD), Fourier Transform Infrared (FTIR), Thermogravimetric analysis (TGA), and Brunauer–Emmett–Teller (BET). Computational modelling using Gaussian 16 was employed to provide qualitative electronic insight into the system. The encapsulation efficiency (EE%) of AChE within the ZIF-8 matrix was found to be 97.60%, which indicates highly effective enzyme loading and confirms the suitability of ZIF-8 as a robust carrier for enzyme immobilization. Acetylcholine (ACh) is catalysed by acetylcholinesterase to produce choline, which results in gold nanoparticles aggregating and a corresponding colour change. Under optimal conditions (temperature: 37 °C, buffer pH: 7.6, incubation time: 20 min, and ACh concentration: 4 mmol/L), the colour change can be employed for the detection of carbamate pesticides at low concentrations, with rapid sensitivity for carbaryl detection at a detection limit of 4.95 nM, and shows consistent performance in the analysis of spiked real water samples, achieving recoveries of 92.2–103.3%. AChE@ZIF-8 exhibits strong stability during biological storage, making it feasible for on-site carbaryl detection and showing great potential for wider applications in water pollutant monitoring.

Keywords Acetylcholinesterase · Acetylcholine · AuNPs · Encapsulation · ZIF-8 · Pesticides

✉ Fazira Ilyana Abdul Razak
fazirailyana@utm.my

✉ Shahrul Ainliah Alang Ahmad
ainliah@upm.edu.my

[1] Institute of Nanoscience and Nanotechnology, Universiti Putra Malaysia, 43400 Serdang, Selangor, Malaysia

[2] Department of Chemistry, Faculty of Science, Universiti Putra Malaysia, 43400 Serdang, Selangor, Malaysia

[3] Centre of Foundation Studies for Agricultural Science, Universiti Putra Malaysia, 43400 Serdang, Selangor, Malaysia

[4] Department of Chemistry, Faculty of Science, Universiti Teknologi Malaysia, 81310 Skudai, Johor, Malaysia

[5] Pusat Pengajian Kimia dan Alam Sekitar, Fakulti Sains Gunaan, Cawangan Negeri Sembilan, Kampus Kuala Pilah, Universiti Teknologi Mara, 72000 Kuala Pilah, Negeri Sembilan, Malaysia

[6] Department of Physics, Faculty of Science and Technology, Universitas Airlangga, Surabaya, Indonesia

Introduction

The application of pesticides has been a great contribution to improve agricultural productivity and soil fertility by controlling pest insects [1]. They have been widely used to control mosquitoes, ticks, cockroaches, rodents, fleas, and other dangerous pests in agricultural areas and houses [2]. These chemicals are commonly found in soil, air, groundwater, and agricultural products [3]. However, the negative effects of pesticides have led to public concern on health, the environment, and food safety [4]. 1-Naphthyl methylcarbamate (carbaryl) is a broad-spectrum N-carbamate-based insecticide that has been extensively used around the globe [5]. Carbaryl is highly toxic because it could persistently block the function of acetylcholinesterase (AChE) in central and peripheral nervous systems, which prevents the transmission of neurotransmitter, finally leading to death [6]. Carbaryl has been prohibited in most countries of the European Union [7].

Published online: 12 August 2026

This phenomenon is because carbamate residues in meals act as acetylcholinesterase inhibitors, which can cause long-term harm to the brain, neurological system, liver, muscles, and pancreas [8]. The extensive and often indiscriminate use of pesticides in agricultural products has amplified the demand for quick residue analysis methods [9].

Conventional approaches like gas chromatography, high-performance liquid chromatography (HPLC) or coupled ones like gas chromatography–mass spectrometry (GC–MS) are currently used as standard methods to detect pesticide residues in the agricultural sector. In previous work, simultaneous monitoring of exposure to two N-methylcarbamate pesticides, carbaryl (CRB) and carbofuran (CF) pesticides and their metabolites was performed using a gas chromatographic–tandem mass spectrometric (GC–MS/MS) method, highlighting the need for specific biological monitoring methods to evaluate dermal and inhalation exposure to these pesticides [10]. For the simultaneous detection of 102 pesticide residues in green tea, Huang et al. [11] developed and verified a modified QuEChERS (quick, easy, cheap, effective, robust, and safe) technique in conjunction with high-performance liquid chromatography–tandem mass spectrometry (HPLC–MS/MS). These techniques have low limits of detection and excellent selectivity but require costly chemicals, lengthy sample pre-treatment, or expert operators and sophisticated apparatus, limiting their use. These methods have been standardized; none of them is appropriate for on-site screening and rapid detection of pesticides [12]. Alternative solutions are highly desirable to overcome the limitations of the current techniques and to meet future detection requirements.

A biosensor utilizing acetylcholinesterase (AChE) inhibition was created in 1980 to identify carbamate pesticides [13] due to its capacity for on-site screening with straightforward sample preparation, requiring minimal sample quantities and enabling both quantitative and qualitative assessments of pesticide compounds through specific reactions and chosen signals [14]. Colorimetric sensing strategies have been the subject of extensive research in the field of analysis due to their many benefits, including their ease of use, inexpensiveness, high sensitivity, direct measurement, and ability to be detected with a simple UV–vis spectrometer or even just the naked eye [15]. Gradually, a colorimetric AChE assay utilizing nanoparticles of gold and silver has been developed. For instance, D. B. Liu et al. reported a novel gold nanoparticle-based dual-readout analysis for organophosphorus and carbamate pesticides. Regrettably, the natural enzymes used are extremely sensitive in hostile settings, resulting in a lack of robustness in these enzyme-based biosensors in practical applications [16], and their storage issue has become an important constraint to their potential to establish good detection tools [17].

To circumvent some of the limitations above, attention has started to focus on designing a nanoreactor-like environment for the encapsulated enzyme. The MOF encapsulation technique has contributed greatly to the enhancement of enzyme lifespan and protection like heat stability, pH stability, organic solvent stability [18], storage stability, and recyclability [19] when compared to conventional immobilization strategies. It is also worth noting that the zeolitic imidazolate framework-8 (ZIF-8), which is made up of Zn^{2+} nodes and 2-methylimidazole (2-MIM) connections, is a well-developed and widely utilized MOF at the current time [20], likely due to its amenability to biocompatible synthesis [21]. For instance, ZIF-8 has the potential to inhibit conformational changes in enzymes and create an optimal microenvironment for enzyme accommodation. Lyu et al. presented a cytochrome C/ZIF-8 composite demonstrating a tenfold enhancement in bioactivity relative to the free enzyme in reducing H_2O_2 [22]. Kukkar et al. incorporated AChE into ZIF-8 to form AChE@ZIF-8 for the detection of organophosphate pesticides [23], whereas Cao et al. packaged multi-enzymes (AChE, HRP, and CHO) into CF-ZIF-8 for the detection of acephate in Chinese cabbage and romaine in blood [24]. AChE@ZIF-8 composites have been reported previously for organophosphate pesticide detection; their application for carbaryl (carbamate) sensing remains limited. In addition, most reported systems rely on conventional synthesis routes that often involve organic solvents, which may affect enzyme activity and raise environmental concerns. Therefore, there is a need to develop a greener and biocompatible synthesis approach for AChE immobilization while evaluating its performance for carbaryl detection. In this work, a water-based in situ synthesis of AChE@ZIF-8 was developed and integrated with an AuNP-based colorimetric sensing platform for carbaryl analysis.

The in situ encapsulation of AChE was performed in this study using deionized water as a mild and environmentally friendly synthesis medium, thereby avoiding toxic organic solvents such as DMF and methanol. This method allows the enzyme to keep its activity and to be effectively immobilized within the framework. A supplementary computational study using Gaussian 16 was conducted to support the experimental observations. The results provide qualitative insight into enzyme–framework interactions and are consistent with the improved stability observed experimentally.

The potential applicability of the ZIF-8-based system for sensitive and selective carbamate pesticide biosensing was evaluated using gold nanoparticles (AuNPs) as a colorimetric sensor probe due to their strong localized surface plasmon resonance (LSPR) properties. At neutral pH, choline carries a positive charge, which facilitates electrostatic-induced aggregation of AuNPs. By monitoring the plasmonic resonance of nanoparticles, such aggregate development may be simply monitored and identified using

UV–Vis and naked eyes based on the colour change (red colour of AuNPs changes to blue). AChE activity is inhibited in the presence of a pesticide such as carbaryl, and ACh cannot be converted into choline. As a consequence, the AuNPs will stay distributed in the solution as individual particles rather than creating aggregates (the colour of AuNPs remains red) (Fig. 1). For quantitative analysis, a reverse correlation between AuNP aggregation and pesticide concentration can be established.

Materials and methods

Chemicals and instruments

Zinc nitrate hexahydrate ($Zn(NO_3)_2.6H_2O$, 99% purity), Acetylcholinesterase from *Electrophorus electricus* (electric eel; Type VI-S, lyophilized powder, 200–1000 units/mg protein), 2-methylimidazole ($CH_3C_3H_2N_2H$, HmIm, 99% purity), acetylcholine chloride (ACh; molecular weight = 181.66 g/mol). Carbaryl ($C_{10}H_7OCONHCH_3$), Bradford's reagent, and Bovine Serum Albumin (BSA) were purchased from Sigma-Aldrich (USA). Tris–HCl buffer solution (ultra-pure grade) was purchased from Vivantis Biochemical. Colloidal Gold from Kestrel BioSciences (Thailand) Co., Ltd. Deionized water (18.2 MΩ cm at 25 °C, Milli-Q) was used throughout the experiments. All chemicals and reagents were commercially available.

X-ray powder diffraction (PXRD, XRD-6000, Shimadzu, Japan) was used for the phase identification of crystalline material, utilizing a diffractometer equipped with a CuKα source, a scan step of 0.05°, a counting time of 20 s per step, and a scan range of 3° to 50°. For sufficient particle participation in the diffraction procedure, the analysed sample must be precisely ground and homogenized. The surface area was investigated by Brunauer–Emmett–Teller (BET, Micromeritics Tristar II Plus, USA). The samples were degassed for 4 to 12 h at 50 °C and weighed. At 77 K and 0.1 mbar final pressure, nitrogen gas was evacuated to plot the adsorption and desorption isotherms, revealing the compound's adsorption capacity. Ultraviolet–visible (UV) spectrophotometer (UV–Vis, Lambda 35 UV–Vis spectrometer, Perkin Elmer USA) to record the absorbance peak of colorimetric detection in the range wavelength of 300 to 800 nm. To achieve a transparent solution, the sample was diluted with a suitable solvent and placed into cuvettes. The chemical functionalities in synthesized substances and changed surfaces were determined by Fourier transform infrared (FTIR, Nicolet 6700, Thermo Nicolet Corp). To achieve a transparent solution, the sample was diluted with a suitable solvent and placed into cuvettes (Madison, WI, USA). The sample was carefully dried beforehand to minimize the water content.

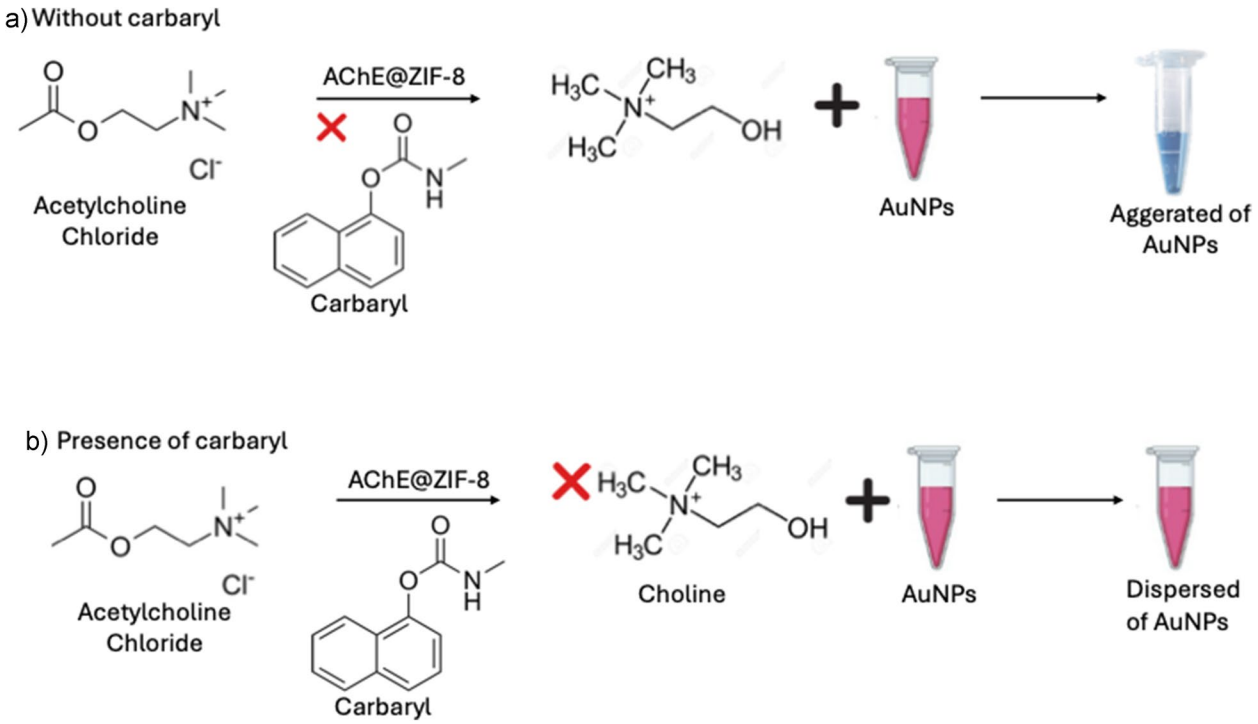

Fig. 1 Mechanism of carbaryl detection using an AuNPs biosensing system. **a** In the absence of carbaryl, the hydrolysis of acetylcholine (ACh) to choline, which induces AuNP aggregation. **b** In the presence of carbaryl, the inhibition of AChE activity prevents the production of choline and maintains the dispersion of AuNPs

On the sample, the equipment employed infrared radiation ranging from 10,000 to 100 cm^{-1}. The sample molecules transform the absorbed radiation into vibrational or rotational energy, and the resulting signal is shown as a 4000 to 500 cm^{-1} spectrum. Thermogravimetric analysis (TGA; Mettler Toledo model STARe SW, Switzerland) was used to determine the weight loss of the synthesis compound. The minimum sample weight of 5 to 20 mg was placed in an alumina crucible and heated while its weight was monitored on an analytical balance that was kept outside of the furnace. The gas sorption was carried out in an oxygen environment at 77 K with a heating rate of 5 °C/min from 50 to 800 °C. Field emission scanning microscopy (FESEM, Nova Nano SEM 230, USA) to capture the morphology of the materials. The thin gold layer was deposited on each sample under the high-vacuum conditions. Carbon tape was then used to secure the sample to the substrate. To obtain pictures at a bar of 500 nm, an accelerating voltage of 5 kV was used, and magnification in the range of 10 kx to 100 kx was used.

Green synthesis of encapsulation AChE@ZIF-8

The synthesis of AChE@ZIF-8 was prepared in a water solution at room temperature using the previous procedures with slight modifications [17]. In brief, AChE (0.08 mg/mL, 750 µL) and $Zn(NO_3)_2.6H_2O$ solution (0.31 M, 250 µL) were mixed with a 2-methylimidazole solution (HmIm; 2.5 M, 2.5 mL), and then aged for 30 min at room temperature. After mixing, a milky solution was formed instantly. The product was collected by centrifugation at 10,000 rpm for 15 min, then washed three times in deionized water and redissolved in 5 mL of deionized water. The pure ZIF-8 compound was synthesized using the same method but without the addition of the enzyme AChE to the HmIm solution. The obtained products were dried using freeze-drying before being characterized.

Computational details

The crystal structure of ZIF-8 was based on the material crystallographic information file from the Cambridge Crystallography Data Centre (CCDC code: 864309). ZIF-8 crystallizes in cubic space group I-43 m with lattice parameters $a = b = c = 16.8509$ Å, angles $\alpha = \beta = \gamma = 90°$ and a unit cell volume of 4784.09 Å. The acetylcholinesterase model was also based on data from its crystal structure, which was obtained from the RCSB Protein Data Bank (PDB code: 1EVE). It is noted the water molecules present in the crystal structure of acetylcholinesterase were removed prior to carrying out the simulations.

All quantum-chemical calculations were performed using Gaussian 16 [25], and the resulting structures were visualized with GaussView 6.0 [26]. Geometry optimizations were carried out in the gas phase using unrestricted DFT with the B3LYP hybrid functional. A mixed GEN scheme was adopted in which the LANL2DZ effective core potential was used for the Zn centre, while the 6-311G (d,p) basis set was applied to all other atoms [27–29]. Frequency calculations were used to confirm that the optimized geometries corresponded to true minima, as indicated by the absence of imaginary frequencies. Frontier molecular orbitals (HOMO–LUMO) and molecular electrostatic potential (MEP) surfaces were subsequently evaluated at the same level of theory, with visualizations generated in GaussView 6.0. All calculations were conducted using the High-Performance Computing (HPC) facilities provided by the Center for Information and Communication Technology (CICT), Universiti Teknologi Malaysia (UTM).

Encapsulation efficiency (EE%)

The encapsulation efficiency (EE%) of AChE@ZIF-8 was assessed using the Bradford assay. The Bradford assay was carried out by mixing Coomassie Brilliant Blue G-250 reagent with the protein sample at a 1:10 (v/v) ratio. A shift in the absorbance maximum from 465 to 595 nm was observed as the acidic dye solution bound with the protein, resulting in a colour range from reddish brown to blue. Bovine serum albumin (BSA) was used as the standard protein for calibration. The concentration of acetylcholinesterase (AChE) and supernatant AChE@ZIF-8 was determined spectrophotometrically. The encapsulation efficiency (EE%) of acetylcholinesterase (AChE) into ZIF-8 is calculated using the formula:

$$EE\% = \frac{B - C}{B} \times 100$$

where

B Initial protein content

C Unbound protein (supernatant)

Optimization conditions and enzymatic activity

The optimization of parameters influencing the enzymatic activity of free enzyme (AChE) and AChE@ZIF-8 was performed. These parameters include the pH of the working buffer, the incubation time of enzymatic hydrolysis, and the corresponding concentrations of ACh, involving the utilization of the absorbance of AuNPs.

A slightly modified methodology from (Shah et al., 2021) was used to determine the hydrolysis of ACh by the AChE@ZIF-8 composite. 20 mM Tris–HCl buffer (pH 7.5) was used in the preparation of stock solution (1 mg/mL) and working

solution (0.08 mg/mL) of AChE@ZIF-8. The solution of substrate ACh (4.0 mmol/L) was prepared with water. Following this, 150 µL of Tris–HCl buffer (100 mM, pH 7.6), 75 µL of AChE (0.08 mg/mL), and 4.0 mmol/L of 60 µL ACh in a microcentrifuge tube and incubated for 20 min at 37 °C. After that, 60 µL of the AuNPs colloidal solution (20 nM) and 60 µL of the above solution were well mixed. The UV–vis spectra of the resulting solutions were examined, as well as the reduction in absorbance at 520 nm and the new peak appearing at 650 nm depicted the enzymatic activity occurring.

Sensitivity and selectivity studies

The sensitivity of AChE@ZIF-8 was evaluated by incubating AChE@ZIF-8 with different concentrations of carbaryl ranging from 20 to 160 nM. The limit of detection (LOD) was determined from the calibration curve of carbaryl concentration versus the A520/A650 absorbance ratio. For the selectivity study, carbaryl in the 100 mM Tris–HCl buffer solution (pH 7.6) was individually replaced with potential interfering species (K^+, Pb^{2+}, Hg^{2+}, Cu^{2+}, As^{3+}, and atrazine) at the same concentration, and their responses were evaluated for activity determination.

Colorimetric detection of carbaryl using a gold nanoparticle (AuNP) probe

The neurotoxin of carbaryl insecticide was tested as an inhibitor of the AChE@ZIF-8 composite with the slight modification methodology [30]; 150 µL of Tris–HCl buffer (100 mM, pH 7.6), 25 µL of AChE (0.08 mg/mL) and various dilutions of the carbaryl (from 20 nM to 160 nM) were combined and incubated at 37 °C for 10 min. Next, 20 µL of ACh (4 mmol/L) was added to each sample, and the reagents were incubated for another 20 min followed by 60 µL of AuNPs and 60 µL of the above solution. The inhibitory activity of AChE@ZIF-8 was determined by various concentrations of carbaryl pesticide (from 20 nM to 160 nM).

Carbaryl detection in water samples

The water samples were pre-treated by filtration through a 0.45 µm membrane filter to remove particles that could clog the HPLC system and interfere with the analysis. Subsequently, 30 mL of methylene chloride was added to a 250 mL separatory funnel containing 100 mL of the water sample, and the mixture was shaken vigorously for 2 min. The organic solvent was transferred into a clean 100 mL volumetric flask when two layers were separated in separatory funnel and diluted to the mark with methylene chloride. The extract sample was filtered with 0.45 µm membrane filtration and spiked with 10, 20 and 30 µM concentrations of standard carbaryl.

An Agilent Technologies 1200 series high-performance liquid chromatography (Germany) equipped with an Agilent 1200 quaternary pump, diode array detector, autosampler, and Chemstation for LC software was used for the analysis. The analytical column used in the experiment was a ThermoHypersil column (Sweden) C18 (250 mm X 4.6 mm). The mobile phase was a 100% phosphate buffer solution (0.1 M, pH 7.4) that had been filtered and degassed. The flow rate was set to 0.5 mL/min and the detector wavelength was set at 292 nm with an injection volume of 10 µL.

Result and discussion

Characterization of AChE@ZIF-8

The crystallinity structure of ZIF-8 and AChE@ZIF-8 was assessed by powder X-ray diffraction (PXRD) analysis. Fig. S1a depicts the peak at 2θ values of 7.3°, 10.4°, 12.7°, 14.8°, 16.5° corresponding to planes (011), (002), (012), (022), respectively. These results match with simulated ZIF-8 [31], demonstrating the PXRD pattern did not change with encapsulation of AChE within ZIF-8. This indicates that the crystalline structure was maintained after encapsulation [17]. For the FTIR result (Fig. S1b), a band at 2931 cm^{-1} can be clearly seen in all samples, which can be assigned to the characteristic C-H bond vibration. Apart from the C-H absorption band, the bands at 1573 cm^{-1} (C=N stretching vibration) and 1140 cm^{-1} (C-N stretching vibration) were also observed for bare ZIF-8 and AChE@ZIF-8. The amide I group, observed at 1645 cm^{-1}, corresponds to the C=O stretching vibration of peptide linkages, while the band around 1500–1600 cm^{-1} is attributed to the amide II group, which consists of N–H bending and C-N stretching vibration and provides information on the secondary structure of the enzyme [32]. All these characteristic bands of the bare ZIF-8 nanoparticles were also present in the AChE@ZIF-8 nanoparticles. The similarities in FTIR spectra (before and after encapsulation) confirm the successful encapsulation of AChE within ZIF-8 without disrupting the framework [33].

Both ZIF-8 and AChE@ZIF-8 were placed underneath TGA in order to measure their thermal stability. As shown in Fig. S1c, the decomposition of ZIF-8 and AChE@ZIF-8 started with a weight loss of 20–30% under a nitrogen environment as the temperature was increased to 200 °C. This weight loss percentage is attributed to the removal of solvents such as H_2O and excess residues in the ZIF-8 structure after being heated overnight. After the first decomposition, constant weight was observed in the temperature range from 300 to 500 °C, indicating

high thermal stability of the ZIF-8 structure. The second decomposition of both ZIF-8 and AChE@ZIF-8 occurs up to 600 °C, which is contributed to the decomposition of organic linker, 2-MeIm and ZIF-8, which leads to the formation of zinc oxide (ZnO) as the final calcination product of ZIF-8 crystals [2]. Furthermore, for AChE@ZIF-8, a relatively lower initial decomposition temperature around 180 °C is observed. The resulting decomposition occurs due to the thermal instability of the AChE enzyme and the decreased concentration of Zn metal sites upon encapsulation 23.

In addition, N_2 adsorption–desorption isotherms and a pore size distribution curve were used to analyse the porous nature of ZIF-8 and AChE@ZIF-8. ZIF-8 and AChE@ZIF-8 exhibited a type I isotherm [18], as shown in Fig. S1d. Due to the micropores, the adsorption capacity at low relative pressure ($P/P_0 < 0.1$) was exceptionally high. The BET surface area of ZIF-8 was 2486.62 m^2/g, which significantly decreased to 1419.74 m^2/g after AChE encapsulation. This reduction, approximately 43% strongly indicates that AChE molecules have been successfully immobilized within the porous framework of ZIF-8, effectively occupying internal spaces and reducing accessible adsorption sites. Similarly, the total pore volume of ZIF-8 decreased from 0.7449 cm^3/g to 0.4268 cm^3/g, further supporting the idea that enzyme molecules have been confined within the pore channels, partially blocking nitrogen adsorption. This substantial decrease in pore volume confirms that AChE is not merely adsorbed on the external surface but is effectively incorporated inside the pores, altering the internal porosity of ZIF-8.

The morphology and particle size distribution of ZIF-8 and AChE@ZIF-8 were examined using FESEM, as shown in Fig. S2. According to the findings, pure ZIF-8 and AChE@ZIF-8 have the same shape, defined by a rhombic dodecahedron structure. ZIF-8 had a lower particle size distribution (85–90 nm) than AChE@ZIF-8 (95–105 nm). The rise in particle size is considered indicative of a successful in-situ biomimetic process. According to Liang et al., the biocomposite was formed primarily by protein binding with metal ions or organic ligands to form nanosize aggregates, which then induced the nucleation of ZIF crystals as outer protective shells, increasing the robustness of the biomolecules [34]. This shows that protein stabilization was facilitated by the coordination of Zn(II) ions with the protein's amide bond, as well as weak interactions such as hydrogen bonding and hydrophobicity of amino acids with the hydrophobic interior of the imidazole-containing building block of ZIFs [35, 36].

Although surface adsorption of enzymes on the ZIF-8 surface cannot be completely excluded, the structural characterization results obtained from PXRD, FTIR, and TGA indicate that AChE was successfully encapsulated within the ZIF-8 framework during the biomineralization process. The preservation of the crystalline structure further confirms that the MOF framework was not disrupted.

Computational studies

Molecular electrostatic potential (MEP) and frontier molecular orbital (HOMO–LUMO) analyses were performed using Gaussian 16 to provide insight into the intrinsic electronic properties of selected AChE catalytic residues and the ZIF-8 framework. The MEP results illustrate the charge distribution of the studied systems, indicating possible electrostatic complementarity at the molecular level (Fig. S3). HOMO–LUMO gap analysis shows variations in energy gaps among the residues, ZIF-8, and residue@ZIF-8 model systems, reflecting differences in their relative electronic properties and chemical reactivity (Fig. S4). These computational results are presented as qualitative electronic descriptors and are not intended to directly represent enzyme–framework interactions, but they complement the experimental observations of AChE@ZIF-8 performance and stability.

Encapsulation efficiency (EE%) of AChE@ZIF-8

UV–Vis spectroscopy was employed to determine the encapsulation efficiency of AChE within the ZIF-8 framework. As shown in Fig. 2, a standard calibration curve constructed using bovine serum albumin (BSA) exhibited a strong linear correlation between protein concentration (mg/mL) and absorbance ($y = 0.7094x + 0.0759$, $R^2 = 0.9804$), confirming the reliability and sensitivity of the method for protein quantification. The inset image demonstrates a progressive intensification of the blue colouration with increasing protein concentration, visually supporting the spectrophotometric results. By comparing the absorbance of unencapsulated AChE in the supernatant with the calibration curve, the concentration of free enzyme was determined, enabling the calculation of the encapsulation efficiency. The obtained

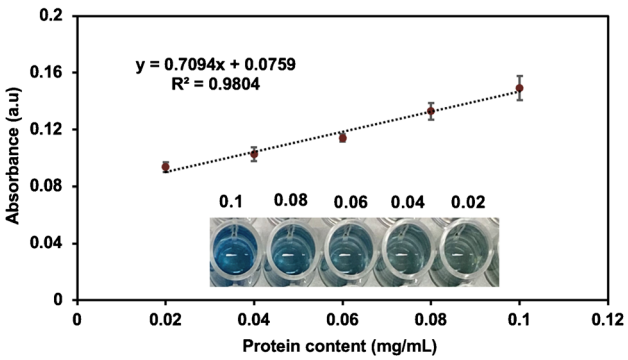

Fig. 2 Calibration curve for different protein concentrations (0.02–0.10 mg/mL)

EE% was 97.6%, indicating highly efficient enzyme loading within the ZIF-8 matrix. This excellent encapsulation efficiency highlights the potential of ZIF-8 as a robust carrier for enzyme immobilization, offering significant promise for applications in biosensing, catalysis, and therapeutic delivery.

Enzymatic activity of AChE and AChE@ZIF-8

The enzymatic activity by AChE@ZIF-8 relative to native AChE was evaluated by aggregation-induced spectral changes of gold nanoparticles (AuNPs) in the terms of pH, temperature, incubation time and ACh concentrations. All experiments were performed in triplicate (n = 3), and results are presented as mean ± standard deviation. The temperature effects on AChE@ZIF-8 and AChE activity were measured at various temperatures (25, 37, 50, 75, and 90 °C) as shown in Fig. 3a. The temperature for both AChE@ZIF-8 and AChE increased as the temperature increased from 25 °C to 37 °C. The optimal temperature for both systems was determined to be 37 °C. However, the peak activity of AChE sharply declined beyond 50 °C, demonstrating the thermal denaturation behaviour, while AChE@ZIF-8 maintained significantly higher activity at elevated temperatures (60–75 °C), indicating increased thermal stability likely due to spatial confinement and reduced conformational flexibility within the ZIF-8 pores. These results demonstrate the significant protective ability of the MOF encapsulation; the framework supports the enzyme at higher temperatures, preventing the proteins from unfolding and denaturing [37]. For parameters' condition of pH buffer (Fig. 3b), the enzyme activity was measured from the range pH (3.6, 5.6, 7.6, 9.6, and 11.6). Under acidic conditions, ZIF-8 is susceptible to deterioration due to the protonation of organic ligands. 2-methylimidazole induces the cleavage of Zn–N links, destabilizing the ZIF-8 framework and resulting in the release of the enzyme [38]. The absorbance change reduced owing to enzyme denaturation in an extremely alkaline environment. Figure 3c shows the comparison in time of incubation between AChE@ZIF-8 and AChE. The effect of incubation time was investigated from 5 to 30 min, and 20 min was selected as an optimal condition for good catalytic activity with a relatively short duration. AChE@ZIF-8 exhibited a higher absorbance within 20 min, whereas AChE required approximately 30 min to achieve a similar response. The best condition for interaction between enzyme and substrate is a concentration 4 mmol/L (Fig. 3d). Beyond a concentration of 6 mmol/L, the graph begins to plateau due to the enzyme reaching saturation. At this point, increasing in the concentration of substrate does not significantly increase the reaction rate.

Kinetics studies of AChE and AChE@ZIF-8

Michaelis–Menten and Lineweaver–Burk plots are two important qualities to consider when assessing the performance of an enzyme (Fig. S5). The Michaelis–Menten describes how the initial velocity (V_0) of an enzymatic reaction depends on the substrate concentration ([S]), following a hyperbolic curve that approaches a maximum velocity (V_{max}) as a substrate saturates the enzyme. The Michaelis constant (K_m) represents the substrate concentration at which

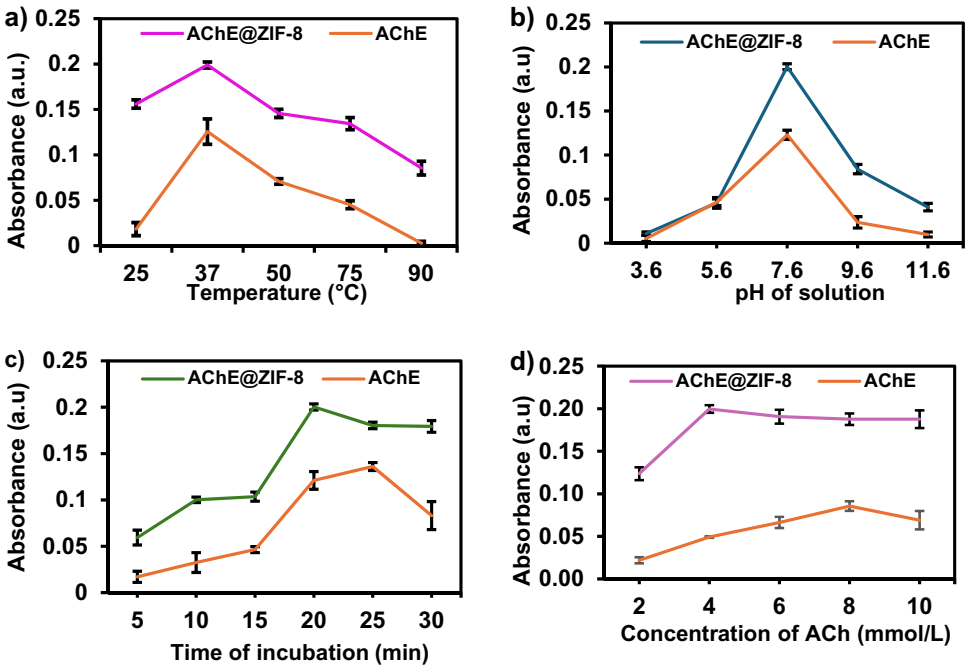

Fig. 3 The optimization conditions of enzymatic activity between AChE@ZIF-8; (**a**) temperature: 37 °C; (**b**) pH of buffer: 7.6; (**c**) time of incubation: 20 min and (**d**) ACh concentration: 4 mmol/L

the reaction velocity is half of V_{max}, reflecting the enzyme's affinity for the substrate. To accurately determine K_m and V_{max} from the experimental data, the Lineweaver–Burk plot linearizes the Michaelis–Menten equation by plotting the reciprocal of velocity ($1/V_0$) against the reciprocal of substrate concentration (1/[S]) [39]. This yields a straight line where the slope equals K_m/V_{max} and the y-intercept equals $1/V_{max.}$ Table 1 demonstrates the summary of kinetic parameters of AChE and AChE@ZIF-8. The Michaelis constant (K_m) values for free AChE (15.11 mmol/L) and AChE@ZIF-8 (16.70 mmol/L) are comparable, suggesting that encapsulation does not substantially affect the enzyme's binding affinity for acetylcholine. This close equivalence suggests that the enzyme's active site remains highly accessible and functionally similar in both free and immobilized states, consistent with substrate molecules effectively reaching the active site without hindrance [23]. The V_{max} values of AChE@ZIF-8 increased by 64.4% (1.71×10^{-3} ΔAbs/min) compared to AChE (1.04×10^{-3} ΔAbs/min), indicating how much better the encapsulated enzyme performs at its maximum catalytic capacity compared to the free enzyme. This increase suggests that encapsulation in ZIF-8 enhances the catalytic efficiency of the enzyme, likely by stabilizing its active conformation and protecting it from denaturation.

Stability studies

To evaluate the protective effect of ZIF-8, the stability of AChE@ZIF-8 compared to the free enzyme was investigated under varying temperature, pH and storage duration. The stability of the immobilized enzyme was measured by monitoring the changes in relative activity % of AChE@ZIF-8 and free enzymes in temperature (25, 37, 50, 75, and 90 °C), pH of buffer (3.6, 5.6, 7.6, 9.6, and 11.6) and over a 30-day period. The samples were stored at 4 °C during the 30-day storage period. All experiments were performed in triplicate (n = 3), and results are presented as mean ± standard deviation. Thermal stability is an important parameter in enzyme immobilization as a strategy to prevent loss of catalytic activity associated with conformational changes at high temperatures [40]. The relative activity of AChE@ZIF-8 and free AChE exhibited similar activity at the optimal temperature of 37 °C (Fig. 4a). However, as the temperature increased up to 90 °C, AChE@ZIF-8 showed significantly higher stability than free AChE. At 90 °C, the retained activity of free AChE was only 2.2%, whereas the encapsulated enzyme retained 44.0% of its initial activity. These results clearly indicate that encapsulation of enzymes in MOFs can prevent conformational changes at high temperatures, thereby enhancing thermal stability [41, 42]. Furthermore, Fig. 4b shows higher relative activity at pH 7.6 for both AChE@ZIF-8 and free AChE. Acidic conditions are not suitable for ZIF-8, leading to framework disintegration, while alkaline conditions are not favourable for the native structure of AChE or biological molecules.

The relative activity of AChE@ZIF-8 remained at approximately 83% after 30 days of storage under the same conditions, as shown in Fig. 6c, whereas the activity of free AChE decreased to approximately 5%. These findings suggest that ZIF-8 enhances enzyme stability under harsh external conditions and extends enzyme shelf life to 30 days. Overall, encapsulation of AChE in ZIF-8 improves thermal stability, pH stability, and storage stability by preventing conformational changes and maintaining enzymatic activity under adverse conditions.

Table 1 Summary of kinetic parameters (K_m, V_{max}) for AChE and AChE@ZIF-8

Kinetic parameters	AChE	AChE@ZIF-8
V_{max} (ΔAbs/min)	1.04×10^{-3}	1.71×10^{-3}
K_m (mmol/L)	15.11	16.70

Colorimetric detection of carbaryl by AChE@ZIF-8

Carbaryl is known to inhibit AChE via binding to the active site of the enzyme. As a result, the hydrolysis of ACh is

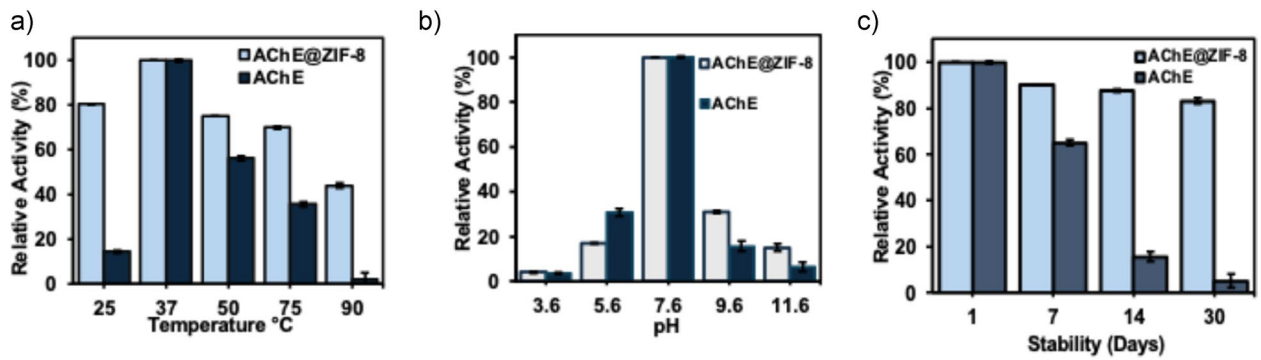

Fig. 4 Stability of AChE@ZIF-8 and AChE in (**a**) thermal stability, (**b**) pH buffer and (**c**) storage over 30 days

inhibited, preventing the formation of choline. This reduced choline minimizes the aggregation of AuNPs, resulting in a simple yet sensitive technique for pesticide detection. AChE catalyses acetylcholine hydrolysis, which yields choline. The positively charged choline causes AuNP aggregation through electrostatic interactions, resulting in a noticeable red-to-blue colour shift. The addition of carbaryl inhibits enzymatic activity, inhibiting choline production and preserving the dispersed AuNP state (red colour).

To exclude the direct effect of ACh on AuNP aggregation, a control experiment was performed by incubating AuNPs with ACh in the absence of AChE. As shown in Fig. S6, no observable colour change was detected, confirming that ACh alone does not induce nanoparticle aggregation. This supports the proposed mechanism (Fig. 1) in which choline is responsible for triggering AuNP aggregation.

To validate the developed biosensors, different concentrations of carbaryl were added to AChE@ZIF-8, and the solutions were combined with ACh and AuNPs. UV–Vis measurements were taken to investigate the colour variations, absorbance spectra, calibration curve of different concentrations of carbaryl, and % inhibition of carbaryl on AChE@ZIF-8.

In the presence of carbaryl, AuNPs remain stably dispersed, maintaining their characteristic red colour. The UV–Vis absorption spectrum exhibits a slightly decreased intensity at 520 nm and no new peak appears around 650 nm. In contrast, absence of carbaryl leads to AuNP aggregation, resulting in a visible colour change from red to blue. This aggregation manifests as a significant reduction in absorbance at 520 nm and the appearance of a new peak around 650 nm, attributed to plasmonic coupling between aggregated nanoparticles. Figure 5a shows the colour of AuNPs in the state of dispersion and aggregation mode and Fig. 5b presents the UV–Vis absorption spectrum of different concentrations of carbaryl in the wavelength range of 300 to 800 nm.

The linearity range and limit of detection (LOD) of the AuNP-based colorimetric assay were examined under optimized experimental circumstances to accurately measure the quantity of carbaryl based on its capacity to block AChE carbamylation. As demonstrated in Fig. 5c, the A520/A650 absorbance ratio increased linearly with increasing carbaryl concentration over the range of 20–160 nM. After graphing the absorbance data (y-axis) against the matching carbaryl concentration (x-axis), a linear regression equation of $y = 0.0090x + 0.4179$ with a coefficient of determination (R^2) of 0.9871 was found. The limit of detection (LOD) was calculated using the equation $LOD = 3\sigma/s$, where σ is the standard deviation of the blank signal and s is the slope of the calibration curve. The LOD of carbaryl in this assay was determined to be 4.95 nM. The analytical performance of the developed AChE@ZIF-8 sensor was further evaluated by comparison with AChE-based and non-enzymatic sensors, which is presented in Table 2. Our AChE@ZIF-8 colorimetric system exhibits a linear correlation ranging from 20 to 160 nM, with a detection limit of 4.95 nM. This performance surpasses that of the AChE–COF electrochemical sensor [43] and the non-enzymatic Ag/ZnO NCs electrode [45]. Significantly, the AChE@ZIF-8 system offers a comparable

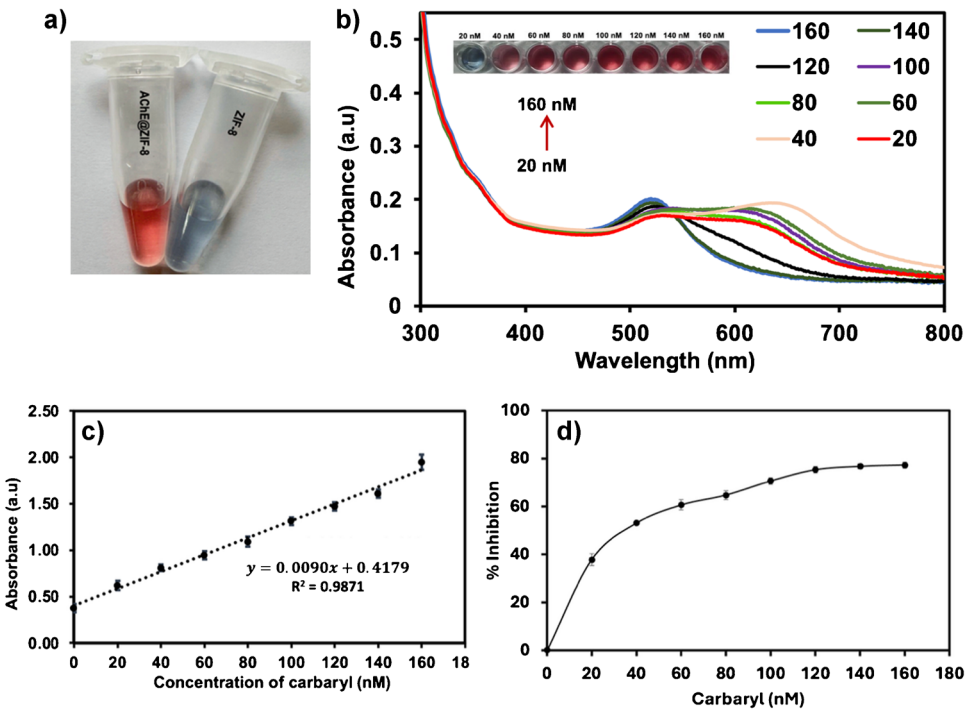

Fig. 5 (**a**) The colour of AuNPs in the state of dispersion (AChE@ZIF-8) and aggregation (ZIF-8) mode in the presence of carbaryl, (**b**) Colour change with increasing concentrations of carbaryl (left to right), together with absorption spectra for carbaryl detection, (**c**) Calibration curve of concentrations of carbaryl (20–160 nM), and (**d**) % inhibition of carbaryl in different concentrations

Table 2 Comparison of reported carbaryl detection methods based on different material systems and analytical techniques

Method	Material/system	Technique	Linear range	LOD	Ref
AChE@ZIF-8	Enzyme–MOF	Colorimetric	20–160 nM	4.95 nM	This work
AChE–COF	Enzyme–COF	Electrochemical	2.2–60 µM	0.22 µM	[43]
MOF–Ag/Au	MOF hybrid	SERS	0.01–20 µg/mL	5.72×10^{-3} µg/mL	[44]
Ag/ZnO NCs	Non-enzymatic	Electrochemical	0.25–100 µM	0.27 µM	[45]
Ag/rGO/CS/AChE	Nanocomposite	Electrochemical	1×10^{-8}–1 µg/mL	1.0×10^{-9} µg/mL	[46]
AuNPs@NO_2	Non-enzymatic	Colorimetric	Not reported	1 µM (UV–Vis) 2 µM (naked eye)	[47]

LOD to the MOF–Ag/Au SERS method [44], offering the practical advantage of colorimetric readout. Detection with the naked eye is only possible with the AuNPs@NO_2 probe [47], though it has a much higher LOD of 2 µM.

Figure 5 d depicts a sigmoidal (S-shaped) dose–response curve illustrating the percentage inhibition of carbaryl towards AChE@ZIF-8. At 0 nM, no inhibition was observed. As the carbaryl concentration increased, the percentage inhibition increased gradually at lower concentrations, indicating partial inhibition of enzyme activity. Between approximately 40 and 80 nM, the curve steepened, reflecting a concentration-dependent inhibition effect. At concentrations above 120 nM, the inhibition continued to increase, suggesting that further increases in carbaryl concentration produced only a minimal additional inhibitory effect. The half-maximal inhibitory concentration (IC_{50}), determined from the sigmoidal dose–response curve, was 36 nM, indicating the carbaryl concentration required to inhibit 50% of the enzyme activity.

The selectivity of AChE@ZIF-8 for carbaryl detection was evaluated against potentially interfering compounds commonly found in physiological fluids, including K^+, Pb^{2+}, Hg^{2+}, Cu^{2+}, Ar^{3+} and atrazine. The selectivity study was performed by individually replacing carbaryl with each potential interfering species at the same concentration in 100 mM Tris–HCl buffer (pH 7.6). As shown in Fig. 6, all interfering species induced only negligible inhibition (< 20%), indicating the high specificity of the proposed sensing platform towards carbaryl [48].

Analysis of real samples and recovery percentage

The validation of carbaryl determination in pond and tap water using the AChE@ZIF-8 biosensor and the reference HPLC method was performed in triplicate (n = 3) to evaluate analytical accuracy and precision. The recovery values obtained with the biosensor ranged from 92.2 to 103.3%, demonstrating satisfactory analytical accuracy for carbaryl detection in both water matrices. Comparable recoveries were obtained using HPLC (94.5–100.6%), indicating good agreement between the two analytical approaches. The slightly higher recoveries observed in tap water compared

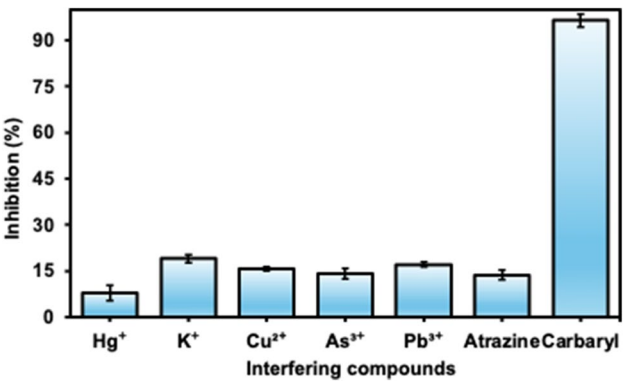

Fig. 6 Inhibition percentage of interfering compounds by AChE@ZIF-8

with pond water can be attributed to reduced matrix interferences, highlighting the influence of sample composition on analytical performance.

The relative standard deviation (RSD) values for both the biosensor and HPLC methods were below 2.0%, confirming good precision and repeatability across triplicate measurements. Such low RSD values are generally considered acceptable for recovery studies involving environmental samples. The consistency of the results across replicates demonstrates the reproducibility of the AChE@ZIF-8 biosensor. As expected, HPLC exhibited lower RSD values owing to its higher instrumental precision. However, the comparable RSD values obtained with the biosensor indicate stable and reliable performance in different water matrices.

A statistical comparison between the biosensor and HPLC results was conducted using a *t*-test at the 95% confidence level. In all cases, the calculated *t*-values were lower than the corresponding critical value, indicating no statistically significant difference between the two methods for carbaryl determination. This statistical agreement further confirms the reliability of the AChE@ZIF-8 biosensor and validates its analytical performance relative to the established HPLC method.

Overall, the results obtained from triplicate analyses demonstrate consistent analytical behaviour rather than random variation. The AChE@ZIF-8 biosensor exhibits

Table 3 Data validation of carbaryl in water samples using AChE@ZIF-8 in comparison with the HPLC conventional instrument

Water sample	Added (μM)	Biosensor found (μM)	Recovery (%)	RSD (%)	HPLC found (μM)	Recovery (%)	RSD (%)	t-test
Pond water	10	9.22	92.2	1.9	9.45	94.5	0.26	1.17
	15	14.11	94.1	1.4	14.58	97.2	0.71	1.36
	20	19.38	96.9	1.6	19.71	98.6	0.62	1.28
Tap water	10	10.33	103.3	1.7	10.06	100.6	0.75	1.41
	15	15.19	101.3	1.3	14.97	99.8	0.68	1.33
	20	19.61	98.1	1.1	20.04	100.2	0.54	1.52

excellent accuracy, precision, and reproducibility for carbaryl detection in water samples. Owing to its simplicity, repeatability, and strong agreement with HPLC results, the developed biosensor shows promise as a cost-effective, rapid, and field-deployable alternative for pesticide monitoring. Table 3 summarizes the comparative performance of the AChE@ZIF-8 biosensor and HPLC for carbaryl detection in pond and tap water samples. All real water samples used in Table 3 were pre-filtered (0.45 μm) prior to analysis.

Conclusion

A simple and green biomimetic mineralization strategy was developed to synthesize an AChE@ZIF-8 enzyme system for rapid and selective colorimetric detection of carbaryl. The proposed platform achieved a low detection limit of 4.95 nM and demonstrated good stability, long-term storage capability, and convenient visual readout using AuNPs without the need for sophisticated instrumentation. The selectivity evaluation was limited to a small number of representative interferents within the scope of this study, and further evaluation using a broader range of pesticide compounds is recommended to fully assess the practical applicability of the sensor. Overall, this work presents a sustainable and efficient biosensing platform with potential applications in environmental and food safety monitoring.

Supplementary Information The online version contains supplementary material available at https://doi.org/10.1007/s00216-026-06729-2.

Author contribution Nor Khairun Bariah Kamaruddin: investigation, formal analysis, validation, writing–original draft preparation. Adila Mohamad Jaafar: supervision, writing—review and editing. Fazira Ilyana Abdul Razak: resources, validation, writing—review and editing. Suhaila Sapari*:* software, investigation, writing—review and editing. Shahrul Ainliah Alang Ahmad: conceptualization, supervision, project administration, writing—review and editing.

Funding Open access funding provided by The Ministry of Higher Education Malaysia and Universiti Putra Malaysia. The authors would like to thank the Ministry of Higher Education (FRGS/1/2021/STG05/UPM/02/2) and Kurita Water and Environment Foundation (23Pmy110) for supporting the project.

Data availability All the data generated are available in this study. Additional data and information can be sourced from the cited references and online databases or sources.

Declarations

Conflict of interest The authors declare no competing interests.

References

1. Leong WH, Teh SY, Hossain MM, Nadarajaw T, Zabidi-Hussin Z, Chin SY, et al. Application, monitoring and adverse effects in pesticide use: the importance of reinforcement of Good Agricultural Practices (GAPs). J Environ Manage. 2020;260:109987.
2. Kaur R, Mavi GK, Raghav S, Khan I. Pesticides classification and its impact on environment. Int J Curr Microbiol App Sci. 2019;8(03):1889–97.
3. Neufeld T, Eshkenazi I, Cohen E, Rishpon J. A micro flow injection electrochemical biosensor for organophosphorus pesticides. Biosens Bioelectron. 2000;15(5–6):323–9.
4. Li H, Guo J, Ping H, Liu L, Zhang M, Guan F, et al. Visual detection of organophosphorus pesticides represented by mathamidophos using Au nanoparticles as colorimetric probe. Talanta [Internet]. 2011;87(1):93–9. Available from: https://doi.org/10.1016/j.talanta.2011.09.046.
5. Lee MG, Patil V, Na YC, Lee DS, Lim SH, Yi GR. Highly stable, rapid colorimetric detection of carbaryl pesticides by azo coupling

reaction with chemical pre-treatment. Sens Actuators B Chem. 2018;261:489–96.
6. Yi Y, Zhu G, Liu C, Huang Y, Zhang Y, Li H, et al. A label-free silicon quantum dots-based photoluminescence sensor for ultrasensitive detection of pesticides. Anal Chem. 2013;85(23):11464–70.
7. Fan Y, Lai K, Rasco BA, Huang Y. Determination of carbaryl pesticide in Fuji apples using surface-enhanced Raman spectroscopy coupled with multivariate analysis. Lwt [Internet]. 2015;60(1):352–7. Available from: https://doi.org/10.1016/j.lwt.2014.08.011.
8. Oliveira TMBF, Ribeiro FWP, Sousa CP, Salazar-Banda GR, de Lima-Neto P, Correia AN, et al. Current overview and perspectives on carbon-based (bio)sensors for carbamate pesticides electroanalysis. TrAC - Trends Anal Chem [Internet]. 2020;124:115779. Available from: https://doi.org/10.1016/j.trac.2019.115779.
9. Kim GY, Shim J, Kang MS, Moon SH. Optimized coverage of gold nanoparticles at tyrosinase electrode for measurement of a pesticide in various water samples. J Hazard Mater. 2008;156(1–3):141–7.
10. Petropoulou S-SE, Gikas E, Tsarbopoulos A, Siskos PA. Gas chromatographic–tandem mass spectrometric method for the quantitation of carbofuran, carbaryl and their main metabolites in applicators' urine. J Chromatogr A [Internet]. 2006;1108(1):99–110. Available from: https://www.sciencedirect.com/science/article/pii/S0021967305024520. Accessed 8 Aug 2026.
11. Huang Y, Shi T, Luo X, Xiong H, Min F, Chen Y, et al. Determination of multi-pesticide residues in green tea with a modified QuEChERS protocol coupled to HPLC-MS/MS. Food Chem. 2019;275:255–64. Available from: https://www.sciencedirect.com/science/article/pii/S0308814618316650. Accessed 8 Aug 2026.
12. Weerathunge P, Behera BK, Zihara S, Singh M, Prasad SN, Hashmi S, et al. Dynamic interactions between peroxidase-mimic silver NanoZymes and chlorpyrifos-specific aptamers enable highly-specific pesticide sensing in river water. Anal Chim Acta [Internet]. 2019;1083:157–65. Available from: https://doi.org/10.1016/j.aca.2019.07.066.
13. da Silva MKL, Vanzela HC, Defavari LM, Cesarino I. Determination of carbamate pesticide in food using a biosensor based on reduced graphene oxide and acetylcholinesterase enzyme. Sens Actuators B Chem. 2018;277:555–61.
14. Umapathi R, Sonwal S, Lee MJ, Mohana Rani G, Lee ES, Jeon TJ, et al. Colorimetric based on-site sensing strategies for the rapid detection of pesticides in agricultural foods: New horizons, perspectives, and challenges. Coord Chem Rev [Internet]. 2021;446:214061. Available from: https://doi.org/10.1016/j.ccr.2021.214061.
15. Xu X, Zhang W, Huang J, Xu H. Colorimetric sensors for detection of organophosphorus pesticides in food: from sensing strategies to chemometrics driven discrimination. Trends Food Sci Technol [Internet]. 2024;152:104683. Available from: https://www.sciencedirect.com/science/article/pii/S0924224424003595. Accessed 8 Aug 2026.
16. Liu P, Li X, Xu X, Niu X, Wang M, Zhu H, et al. Analyte-triggered oxidase-mimetic activity loss of Ag3PO4/UiO-66 enables colorimetric detection of malathion completely free from bioenzymes. Sensors Actuators, B Chem [Internet]. 2021;338(March):129866. Available from: https://doi.org/10.1016/j.snb.2021.129866.
17. Aziz SFNA, Salleh AB, Ashari SE, Normi YM, Yusof NA, Ahmad SAA. Designed Mini Protein 20 mimicking uricase encapsulated in ZIF-8 as nanozyme biosensor for uric acid detection. Nanomaterials (Basel). 2022. https://doi.org/10.3390/nano12132290.
18. Liang K, Ricco R, Doherty CM, Styles MJ, Bell S, Kirby N, et al. Biomimetic mineralization of metal-organic frameworks as protective coatings for biomacromolecules. Nat Commun [Internet]. 2015;6:1–8. Available from: https://doi.org/10.1038/ncomms8240.
19. Liang W, Xu H, Carraro F, Maddigan NK, Li Q, Bell SG, et al. Enhanced activity of enzymes encapsulated in hydrophilic metal-organic frameworks. J Am Chem Soc. 2019. https://doi.org/10.1021/jacs.8b10302.
20. Mohammad M, Razmjou A, Liang K, Asadnia M, Chen V. Metal-organic-framework-based enzymatic microfluidic biosensor via surface patterning and biomineralization. ACS Appl Mater Interfaces. 2019;11:1807–20.
21. Tadepalli S, Yim J, Cao S, Wang Z, Naik RR, Singamaneni S. Metal–organic framework encapsulation for the preservation and photothermal enhancement of enzyme activity. Small. 2018;14(7):1–8.
22. Lyu F, Zhang Y, Zare RN, Ge J, Liu Z. One-pot synthesis of protein-embedded metal-organic frameworks with enhanced biological activities. Nano Lett. 2014;14(10):5761–5.
23. Kukkar P, Kukkar D, Younis SA, Singh G, Singh P, Basu S, et al. Colorimetric biosensing of organophosphate pesticides using enzymatic nanoreactor built on zeolitic imdiazolate-8. Microchem J. 2021. https://doi.org/10.1016/j.microc.2021.106242.
24. Cao X, Guo Y, Zhao M, Li J, Wang C, Xia J, et al. An efficient multi-enzyme cascade platform based on mesoporous metal-organic frameworks for the detection of organophosphorus and glucose. Food Chem [Internet]. 2022;381(January):132282. Available from: https://doi.org/10.1016/j.foodchem.2022.132282.
25. Frisch MJ, Trucks GW, Schlegel HB, Scuseria GE, Robb MA, Cheeseman JR, et al. Gaussian 16, revision C.01. Wallingford, CT: Gaussian, Inc.; 2016.
26. Dennington R, Keith TA, Millam JM. GaussView, version 6. Shawnee Mission, KS: Semichem Inc.; 2016.
27. Becke AD. Density-functional thermochemistry. III. The role of exact exchange. J Chem Phys. 1993;98:5648–52.
28. Hay PJ, Wadt WR. Ab initio effective core potentials for molecular calculations. Potentials for transition metal atoms Sc to Hg. J Chem Phys. 1985;82:299–310.
29. Krishnan R, Binkley JS, Seeger R, Pople JA. Self-consistent molecular orbital methods. A basis set for correlated wave functions. J Chem Phys. 1980;72:650–4.
30. Shah MM, Ren W, Irudayaraj J, Sajini AA, Ali MI, Ahmad B. Colorimetric detection of organophosphate pesticides based on acetylcholinesterase and cysteamine capped gold nanoparticles as nanozyme. Sensors (Basel). 2021. https://doi.org/10.3390/s21238050.
31. Tiwari A, Singh A, Garg N, Randhawa JK. Curcumin encapsulated zeolitic imidazolate frameworks as stimuli responsive drug delivery system and their interaction with biomimetic environment. Sci Rep [Internet]. 2017;7(1):1–12. Available from: https://doi.org/10.1038/s41598-017-12786-6.
32. Tutunaru O, Mihailescu CM, Savin M, Tincu BC, Stoian MC, Muscalu GS, et al. Acetylcholinesterase entrapment onto carboxyl-modified single-walled carbon nanotubes and poly (3,4-ethylenedioxythiophene) nanocomposite, film electrosynthesis characterization, and sensor application for dichlorvos detection in apple juice. Microchem J [Internet]. 2021;169:106573. Available from: https://doi.org/10.1016/j.microc.2021.106573.
33. Van Houten J, Barberi RC, King J, Ogata AF. Improving the colloidal stability of protein@ZIF-8 nanoparticles in biologically relevant buffers. Mater Adv. 2024;5(14):5945–57.
34. Liang K, Carbonell C, Styles MJ, Ricco R, Cui J, Richardson JJ, et al. Biomimetic Replication of Microscopic Metal-Organic Framework Patterns Using Printed Protein Patterns. Adv Mater. 2015;27(45):7293–8.
35. Lian X, Fang Y, Joseph E, Wang Q, Li J, Banerjee S, et al. Enzyme-MOF (metal-organic framework) composites. Chem Soc Rev. 2017;46(11):3386–401.
36. Lei Z, Gao C, Chen L, He Y, Ma W, Lin Z. Recent advances in biomolecule immobilization based on self-assembly: organic-inorganic hybrid nanoflowers and metal-organic frameworks as novel substrates. J Mater Chem B. 2018;6(11):1581–94.

37. Singh R, Musameh M, Gao Y, Ozcelik B, Mulet X, Doherty CM. Stable MOF@enzyme composites for electrochemical biosensing devices. J Mater Chem C. 2021;9(24):7677–88.
38. Gao J, Chu W, Ding X, Ding L, Guo Q, Fu Y. Degradation Kinetic Studies of BSA@ZIF-8 Nanoparticles with Various Zinc Precursors, Metal-to-Ligand Ratios, and pH Conditions. ACS Omega. 2023;8(47):44601–10.
39. Gao L, Zhuang J, Nie L, Zhang J, Zhang Y, Gu N, et al. Intrinsic peroxidase-like activity of ferromagnetic nanoparticles. Nat Nanotechnol. 2007;2(9):577–83.
40. Rafiei S, Tangestaninejad S, Horcajada P, Moghadam M, Mirkhani V, Mohammadpoor-Baltork I, et al. Efficient biodiesel production using a lipase@ZIF-67 nanobioreactor. Chem Eng J. 2018;334:1233–41.
41. Zha F, Shi M, Li H, Rao J, Chen B. Biomimetic mineralization of lipase@MOF biocatalyst for ease of biodiesel synthesis: Structural insights into the catalytic behavior. Fuel [Internet]. 2024;357(PB):129854. Available from: https://doi.org/10.1016/j.fuel.2023.129854.
42. Liu X, Qiu M, Zhang Y, Pan J, Zhang W, Guo L. Enzyme immobilization based on reticular framework materials : Strategy , food applications , and prospect. Adv Colloid Interface Sci [Internet]. 2025;344:103589. Available from: https://doi.org/10.1016/j.cis.2025.103589.
43. Luo Y, Wu N, Wang L, Song Y, Du Y. Biosensor based on covalent organic framework immobilized acetylcholinesterase for ratio metric detection of carbaryl. Biosensors. 2022;12(8):625.
44. Pan Y, Zhao P, Cai W, Fang H, Wang X, Zhao J, et al. MOF@Ag/AAB/Au@Ag composite matrix full-dimensional divergence effect-based SERS paper sensor for rapid carbaryl quantification. Food Chem [Internet]. 2025;472:142885. Available from: https://www.sciencedirect.com/science/article/pii/S0308814625001359. Accessed 8 Aug 2026.
45. Le Nhat Trang N, Thi Nguyet Nga D, Tufa LT, Tran VT, Hung T-T, Ngoc Phan V, et al. Unveiling the effect of crystallinity and particle size of biogenic Ag/ZnO nanocomposites on the electrochemical sensing performance of carbaryl detection in agricultural products. RSC Adv [Internet]. 2023;13(13):8753–64. Available from: https://doi.org/10.1039/d3ra00399j.
46. Mashuni M, Ritonga H, Jahiding M, Rubak B, Hamid FH. Highly sensitive detection of carbaryl pesticides using potentio metric biosensor with nanocomposite Ag / r-Graphene Oxide / chitosan immobilized acetylcholinesterase enzyme. Chemosensors. 2022;10(4):138.
47. Yeon C, Yun S, Kim D, Jeong M, Hyuk J, Heon J. Sensors and actuators : B . Chemical facile and rapid colorimetric detection of carbaryl using nitrite-conjugated gold nanoparticles to ensure environmental and consumer safety. Sensors Actuators B Chem [Internet]. 2024;419:136358. Available from: https://doi.org/10.1016/j.snb.2024.136358.
48. Ayaz S, Uluçay S, Üzer A, Dilgin Y, Apak R. A novel acetylcholinesterase inhibition based colorimetric biosensor for the detection of paraoxon ethyl using CUPRAC reagent as chromogenic oxidant. Talanta. 2024. https://doi.org/10.1016/j.talanta.2023.124962.